

Geophysical Research Letters®

RESEARCH LETTER

10.1029/2024GL108714

High-Frequency Tsunamis Excited Near Torishima Island, Japan, Observed by Distributed Acoustic Sensing

T. Tonegawa¹  and E. Araki¹ 

¹Japan Agency for Marine-Earth Science and Technology (JAMSTEC), Yokosuka, Japan

Key Points:

- The continuous records of our distributed acoustic sensing measurement capture tsunami-related signals
- The phase velocity dispersion of the obtained signals matches that of infragravity waves (high-frequency tsunamis)
- The time-series of the tsunami generation obtained by the cable data are consistent with those from nearby absolute pressure gauges

Supporting Information:

Supporting Information may be found in the online version of this article.

Correspondence to:

T. Tonegawa,
tonegawa@jamstec.go.jp

Citation:

Tonegawa, T., & Araki, E. (2024). High-frequency tsunamis excited near Torishima Island, Japan, observed by distributed acoustic sensing. *Geophysical Research Letters*, 51, e2024GL108714. <https://doi.org/10.1029/2024GL108714>

Received 5 FEB 2024

Accepted 6 MAY 2024

Author Contributions:

Conceptualization: T. Tonegawa

Data curation: E. Araki

Formal analysis: T. Tonegawa

Funding acquisition: T. Tonegawa, E. Araki

Investigation: T. Tonegawa

Methodology: T. Tonegawa

Project administration: T. Tonegawa, E. Araki

Resources: E. Araki

Software: T. Tonegawa

Supervision: T. Tonegawa

Validation: T. Tonegawa

Visualization: T. Tonegawa

Writing – original draft: T. Tonegawa

Writing – review & editing:

T. Tonegawa, E. Araki

© 2024. The Author(s).

This is an open access article under the terms of the [Creative Commons Attribution License](https://creativecommons.org/licenses/by/4.0/), which permits use, distribution and reproduction in any medium, provided the original work is properly cited.

Abstract Recent distributed acoustic sensing (DAS) experiments in ocean areas throughout the world have accumulated records for various wavefields. However, there are few tsunami records because tsunami observation depends on the DAS experimental period and its location. From continuous DAS records, we found tsunami signals at a frequency band of 5–30 mHz, which correspond to high-frequency components of tsunamis and their propagation velocities differ from low-frequency tsunamis. We estimated time series of the tsunami excitations at the source using the DAS records, which are consistent with those using records of ocean-bottom absolute pressure gauges. Our study suggests that DAS records can be used for detecting tsunami propagations in the regions where other geophysical instruments are not available, and contribute to elucidating their excitation mechanisms.

Plain Language Summary Using distributed acoustic sensing (DAS) techniques, various types of wavefields, such as earthquake and ocean waves, have been captured by submarine fiber optic cables. However, the recording of tsunamis has been limited, as their observation depends on the timing and location of the DAS experiments. On 8 October 2023, in southern Japan, changes in sea level attributable to tsunamis were detected by tide gauges. Continuous DAS records in southern Japan have enabled the capture of signals associated with these tsunamis. The observed signals exhibit frequency-dependent propagation velocities, which correspond to infragravity waves. These are essentially deep water waves or ocean surface gravity waves, representing the high-frequency components of tsunamis. Using the DAS records alone, we were able to estimate the time-series of the tsunami generation at the source location. The features obtained from the time-series were consistent with those from records of absolute pressure gauges on the seafloor deployed in southwestern Japan. Our findings demonstrate the utility of DAS records in detecting tsunami propagations and also elucidating excitation mechanisms of tsunamis.

1. Introduction

With a high density of channels along the cable, the distributed acoustic sensing (DAS) technique can monitor the horizontal component of strain along the cable direction, which allows us to investigate the spatial variation of wavefields in detail, including on seafloor telecom cables (Lindsey et al., 2019; Sladen et al., 2019; Williams et al., 2019). This technique has been widely used in marine geophysics for sensing distances of 50–120 km from coastlines to investigate seismological subseafloor structures (Cheng et al., 2021; Fukushima et al., 2022; Lior et al., 2022; Spica et al., 2020; Tonegawa et al., 2022; Viens et al., 2022, 2023), hydroacoustic waves (Matsumoto et al., 2021), Scholte wave generation (Spica et al., 2022), ocean surface gravity waves (Williams et al., 2019), and shallow slow earthquakes (Baba et al., 2023). Ocean DAS records were also uploaded to a repository (Spica et al., 2023) as part of a project that collected DAS data for teleseismic events that occurred in February 2023 (Wuestefeld & Wilks, 2019). Xiao et al. (2024) recently detected tsunami signals; however, DAS observations of tsunamis are still limited because they occur infrequently and their observations depend on the dates and locations of DAS experiments.

On 8 October 2023, sea level changes caused by tsunamis were observed in coastal areas in southern Japan, and repetitive T phases, which are hydroacoustic waves with a propagation velocity of 1.5 km/s (e.g., Ewing & Worzel, 1948; Williams et al., 2006), were also observed at least 14 times by ocean-bottom instruments deployed around Japan (Mizutani & Melgar, 2023; Sandanbata et al., 2023). Since October 2, earthquakes with magnitudes of 4–6 have occurred southwest of the Torishima Island, Japan (Figure 1a), and more than 10 earthquakes with magnitudes of 4–5 occurred immediately before the tsunami observation on October 8 (Table S1 in Supporting Information S1). The tsunamis and T phases are considered to have originated near the areas where the seismic

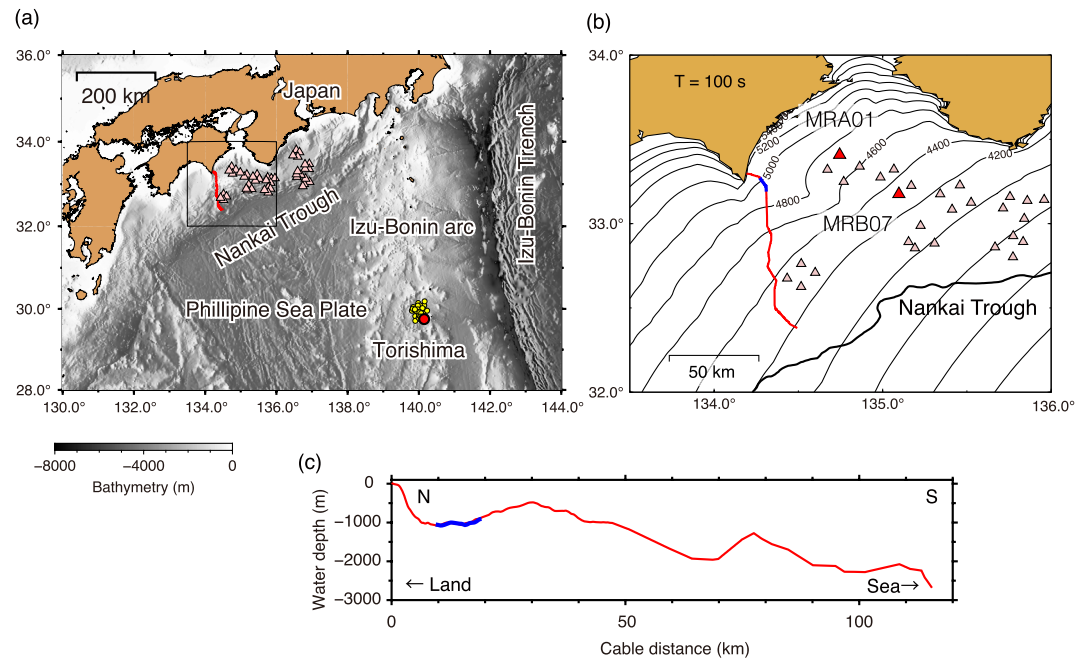


Figure 1. Maps showing the location of the cable and the propagation time of tsunamis. (a) A map showing the locations of seismicity near Torishima Island (yellow circles) (from PDE catalog), the assumed source location (red circle), DONET stations (pale-pink triangles), and the Muroto cable (red line). (b) Contour lines indicate the iso-propagation times of tsunamis for a period of 100 s. Red and blue lines represent the cable and channels of 200–400 (cable distances of 9.8–19.6 km), respectively. Red triangles are the stations of MRA01 and MRB07, respectively. (c) Water depth along the cable.

activity occurred. This area is 300 km west of the Izu-Bonin Trench (Figure 1a), indicating that the excited tsunamis are not caused by large earthquakes around the trench, and the earthquake magnitudes are small to generate tsunamis. Because the epicenters of the seismicity are located in the Izu-Bonin Island arc system, which contains adequate rift zones and submarine volcanoes (Stern et al., 2003; Taylor et al., 1992), the generation of the tsunamis is likely related to geophysical phenomena in such arc-related structures.

We are currently acquiring continuous DAS records using a submarine cable deployed off the Cape Muroto in the southwestern Japan (Figure 1a), around which sea level changes caused by the tsunamis were detected (Mizutani & Melgar, 2023; Sandanbata et al., 2023). In this study, we explore signals corresponding to the tsunamis using continuous DAS records. We compare these signals with waveforms captured by nearby ocean bottom seismometers (OBSs) and absolute pressure gauges (APGs), and investigate their characteristics, including the frequency-dependent phase velocity. Furthermore, we attempt to estimate the energy time function of tsunamis, that is, the time-series of the tsunami energy generation, using DAS and APG records. Such attempts and comparisons contribute to validating whether DAS records are useful for the analysis of tsunamis if cables are deployed without other geophysical instruments. We also discuss possible factors affecting the DAS strain measurement during the tsunami propagation.

2. Data and Methods

2.1. DAS Data

The Muroto cable is 128 km long (Figure 1) with a water depth of 0–2,500 m. A cable section between 0.35 and 2.14 km is buried 0.5–1.0 m below the seafloor, but the other section is unburied. AP Sensing (model N5200 A) acquires the DAS data throughout a sensing length of 120 km along the cable with a gauge length of 78.4091 m. The interrogator measures the differential phase at each channel, and the differential phase can be converted to strain. Detailed descriptions of the cable and AP Sensing observations can be found in Matsumoto et al. (2021) and Ide et al. (2021). The sampling rates of time and space were decimated from 500 to 100 Hz and from 4.9 to 49 m for the processing in this study, respectively. In addition to the cable data, we use OBS and APG records of a permanent cabled network deployed off the coast of southwestern Japan (Dense Oceanfloor Network System for

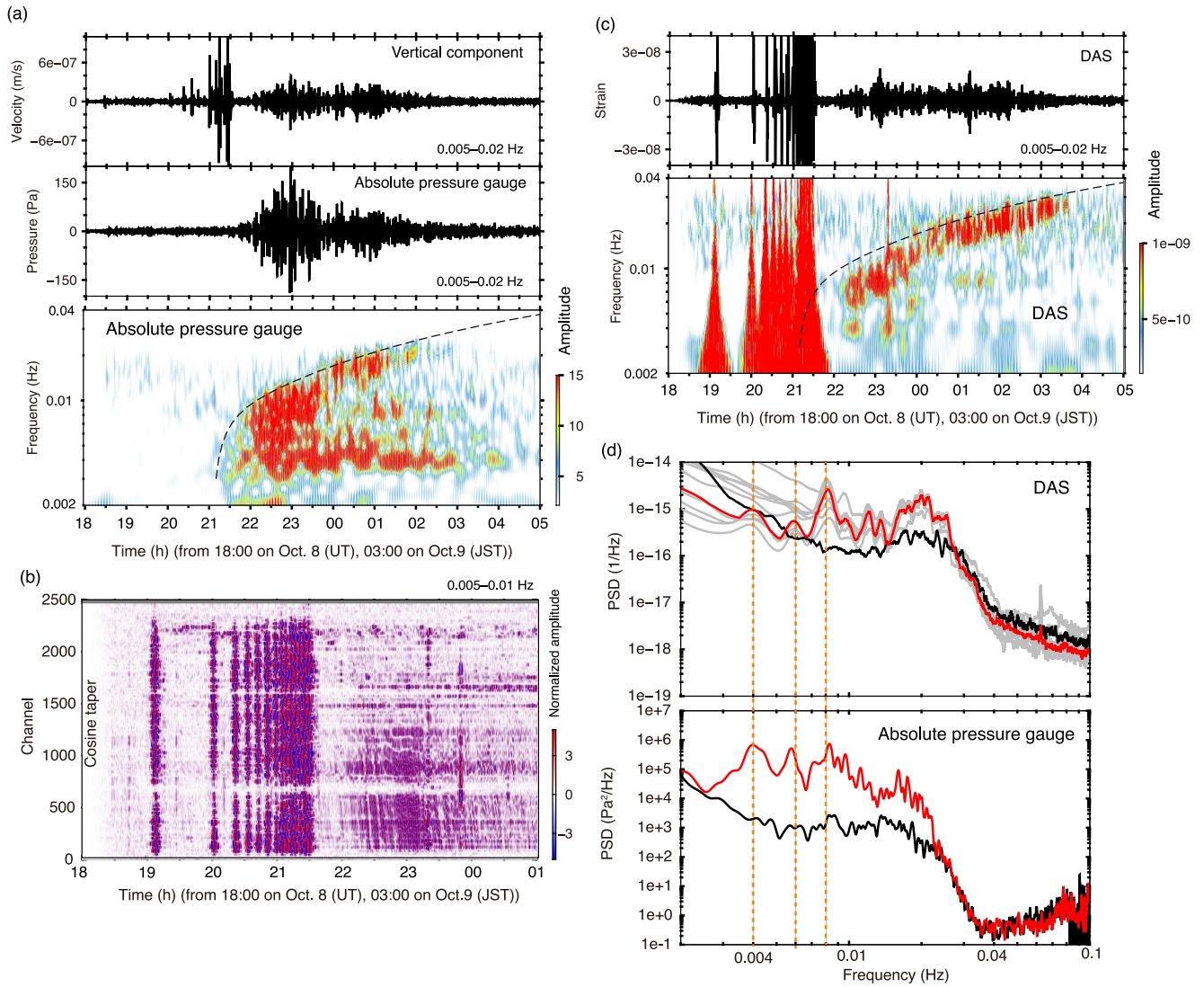


Figure 2. Waveforms and spectra for OBS, APG, and cable. (a) Waveforms in the vertical velocity and the pressure at MRA01 at 5–20 mHz, and the APG spectrogram. Dashed lines correspond to frequency-dependent propagation times for a source location of (29.75°N, 140.15°E) and the origin time of 20:00 (UT). (b) DAS waveforms at 5–10 mHz. Cable distance 0 is located on land. The amplitudes of each trace are normalized by the root-mean-squared amplitude for a time window of 18:30–19:00 (UT). (c) The DAS waveform at 5–20 mHz and spectrogram at a cable distance of 15.435 km. (d) (top) Red and black lines show DAS spectra for the tsunami part (21:40–03:40) and ambient noise part (15:00–18:00), which are the median values for cable distances of 12.25–14.7 km (bottom) Same as the top panel, but for the APG record at MRA01. For each spectrum, the Parzen window with a width of 2 mHz was applied for smoothing. Orange dashed lines correspond to 4, 6, and 8 mHz.

Earthquakes and Tsunamis: DONET) (Aoi et al., 2020; Kaneda et al., 2015; Kawaguchi et al., 2015; NIED, 2019, 2023). The seismometers of the DONET are buried 1 m below the seafloor (Nakano et al., 2013).

Figure 2a shows the waveforms of APG and OBS with a bandpass filter of 5–20 mHz, and the APG spectrogram (MRA01, water depth of 1,375 m). The signal frequency range in the APG spectrum is 2–25 mHz (Figure 2d), which is higher than typical long-period tsunamis caused by large earthquakes. A spindle-shaped waveform and a dispersive feature observed after 22:00 (UT) indicate that the observed signals correspond to high-frequency tsunamis (i.e., infragravity waves (IGWs), deep water waves, ocean surface gravity waves). The arrival times of their long-period components are consistent with the tsunamis observed in the previous studies (Mizutani & Melgar, 2023; Sandanbata et al., 2023). The DAS waveforms and spectrogram show similar features to the high-frequency tsunamis observed by the APG and OBS (Figures 2b and 2c).

Repetitive signals were observed between 19:00 and 21:30 (UT) (4:00–6:30, Oct. 9, JST) in the long-period vertical component of MRA01 (Figure 2a), and the timing of each signal calculated using the origin times of the earthquakes, the distances and the propagation velocity of 1.47 km/s, corresponded to T-phase arrivals. Similar signals are also discernible in the DAS records (Figure 2c), but not in the APG record of MRA01 (Figure 2a). Because the dominant frequency of typical T phase is higher than 4 Hz, the reasons for the generation of such large amplitudes in the long-period components are unclear and are investigated in future studies. We assume in this study that these signals are T-phase-generated site phenomena (T-SP). Although the T-SP obscure the onset part of the spindle-shaped waveforms of the high-frequency tsunamis in the DAS and OBS records, they arrive at ~21:30 in the APG record (Figure 2).

2.2. Propagation Time Calculation of Tsunamis

We calculate the propagation times of IGWs using the method of Tonegawa et al. (2018). For a given angular frequency ω and water depth (H), the phase velocity of IGWs can be estimated by the dispersion relationship (Apel, 1987),

$$\omega^2 = gk \tanh(kH), \quad (1)$$

where k is the wave number, and g is the gravitational acceleration. Using bathymetry data (Smith & Sandwell, 1997) and Equation 1, we assign the phase velocity to each grid ($0.02^\circ \times 0.02^\circ$) within a latitude and longitude range of (28°N – 36°N) and (133°E – 143°E), and calculate the ray paths from a source location (29.75°N , 140.15°E) to the channels of the cable based on the phase velocity map. The source location is approximately determined by the seismicity distribution, and earthquakes on October 8 occurred in the southern part of the seismicity distribution (Figure 1b) (USGS Preliminary Determination of Epicenters (PDE) catalog, (Sipkin et al., 2000)). Here, we used a software FMST (Rawlinson & Sambridge, 2004) to calculate the raypath and the propagation time based on the phase velocity map. Figure 1b shows an example of the propagation times at a period of 100 s. As we also exploit the envelope waveforms with narrow bandpass filters, we integrate the propagation time using the group velocity along each raypath that is calculated using the phase velocity (Tonegawa et al., 2018) (Figure S1 in Supporting Information S1). A narrow-bandpass filter is defined as follows (Dziewonski et al., 1969),

$$H(\omega) = \exp\left\{-\alpha\left(\frac{\omega - \omega_0}{\omega_0}\right)^2\right\}, \quad (2)$$

where ω_0 is the center frequency and α is a parameter for controlling the width of the filter. We used $\alpha = 40$.

2.3. Frequency-Dependent Phase Velocity Estimation

We measure the phase velocities of the dispersive signals to determine if they correspond to tsunamis. We select channels of 200–400 (9.8–19.6 km in cable distance), in which coherent signals are clearly traced (Figure 2b). In this study, records at channels with an increment of 5 within the channel range are used for the subsequent processing. To measure the phase velocity, the arrival times of the signals and their durations should be roughly estimated at each frequency. The duration of large amplitudes is approximately 2 hours (Figure 2). The arrival time of the signals is estimated by both the propagation time based on the group velocity, as explained in the previous section, and the origin time at 20:00. The origin time is determined manually by time-shifting the frequency-dependent propagation time curve and roughly fitting it to the onset of the dispersed signals in the APG spectrogram (bottom panel of Figure 2a). At frequencies where the arrival times are earlier than 22:00, we measure the phase velocity within 2 hours from 22:00 because the T-SP predominated before 21:30. Within the 2 hours, we set a time window of 600 s with 600 s increments (Figure S2a in Supporting Information S1).

We show an example of the phase velocity estimation for a centered frequency of 0.01 Hz (Figure S2 in Supporting Information S1). Using waveforms with a narrow bandpass filter centered at 0.01 Hz (Figure S2a in Supporting Information S1), we calculate the cross correlation function (CCF) between the reference waveform at a channel of 300 and waveforms at other channels of 200–400. An example of the calculated CCFs for one 600-s segment (blue box in Figure S2a in Supporting Information S1) is shown in Figure S2b in Supporting

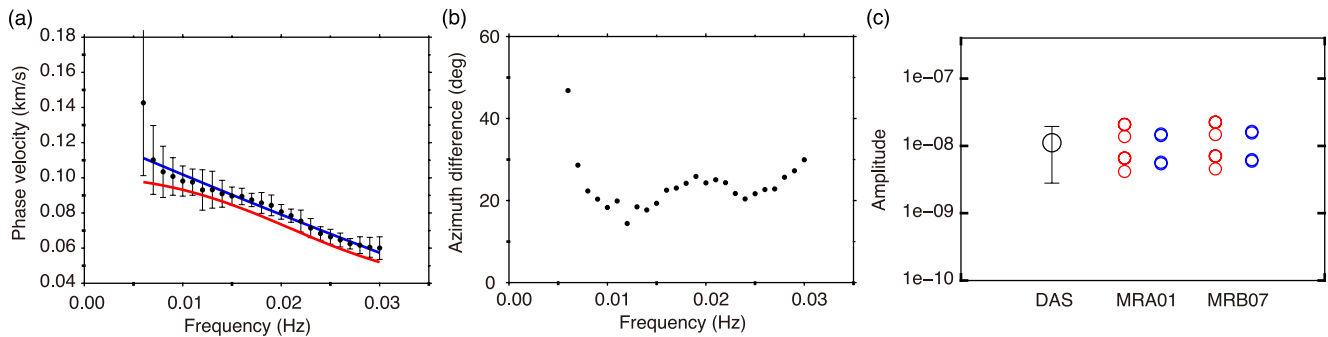


Figure 3. Measurements of properties of tsunami signals. (a) Circles show the measured phase velocities averaged for all of 600-s segments. Blue and red lines are the observed and theoretical dispersion curves for IGWs, in which the observed one is fitted to the circles. (b) The estimated azimuthal difference between the incoming direction of the tsunamis and the cable direction. (c) Red and blue circles indicate the pressure-induced length changes and deformation-induced strains using the maximum pressure amplitudes obtained at MRA01 and MRB07, respectively. Black circle shows the strain of tsunamis derived from the DAS measurement.

Information S1. The gradient of the peaks with significant positive amplitudes flowing through a point at a channel of 300 and a lag time of 0 s represents the phase velocity of the signal. Using a channel spacing of 49 m, we applied a slant stack technique at each time step, stacking the CCF amplitudes by changing the phase velocity. In this case, the phase velocity was estimated as 0.094 km/s (Figure S2c in Supporting Information S1). We repeat this processing between 6 and 30 mHz with a 1 mHz increment and estimate the standard deviation of the calculated phase velocity for all segments within 2 hours. We also calculate the theoretical dispersion curve of IGW propagation using Equation 1 and a water depth of 1,020.5 m which is the averaged water depth for channels of 200–400. These results are presented in Figure 3a.

2.4. Application for Estimating Energy-Time Function

We attempt to reconstruct the frequency-dependent temporal variations in the tsunami energies excited at the source location. The source location is fixed at (29.75°N, 140.15°E) as well. The centered frequencies are 6, 8, 10, 14, 18, 22, 26, 30 mHz. For these frequencies, the total propagation times along the ray paths from the source to the cable are calculated using the group velocity maps. Figures S3a and S3b in Supporting Information S1 show the DAS records with narrow bandpass filters. The amplitudes of the DAS records are time-shifted to the excitation (origin) time using the total propagation time at each channel, which results in the vertically aligned coherent signals (Figures S3c and S3d in Supporting Information S1). The obliquely aligned signals before 20:00 and 21:35 in Figure S3c in Supporting Information S1 and before 19:00 in Figure S3d in Supporting Information S1 are T-SP, and these signals are not related to the tsunami generation. The waveforms in the upper panels of Figures S3c and S3d in Supporting Information S1 are calculated by stacking waveforms at channels of 400–1,000 (19.6–49 km in cable distance), excluding channels of 600–750 that have no coherent signals, and represent the energy-time functions. Similarly, we calculated the energy-time functions at each frequency using APG records from all available DONET stations (water depths ranging from 1,070 to 4,449 m). The amplitudes of these waveforms are normalized by their RMS amplitudes before stacking.

3. Results and Discussion

3.1. Tsunami Dispersion

The signal frequency range in the DAS spectrum is 6–25 mHz (Figure 2d). The APG spectrum shows three peaks at approximately 4, 6, and 8 mHz. Although the 4-mHz peak is comparable to the noise level, the 6- and 8-mHz peaks can be seen in the DAS spectrum. The spectrograms for the DAS (cable distance of 15.435 km, water depth of 1,038 m) and APG records (Figure 2a) exhibit large amplitudes that delay with increasing frequency across a time range of 22:00–03:30 and a frequency band of 5–30 mHz, which indicate that the detected signals show the dispersion feature. The DAS spectrogram shows the amplitudes up to higher frequencies with a longer duration than those in the APG spectrogram (Text S1 in Supporting Information S1). The APG spectrogram shows long-continuing, large amplitudes at 4 mHz, but such signals cannot be identified in the DAS record due to the noise levels.

To confirm whether the dispersive signals are tsunamis, we measured their frequency-dependent phase velocities. The obtained frequency-dependent phase velocities match the theoretical values of IGWs rather than those of long-wavelength tsunamis (Figure 3a). The observed phase velocities, which are slightly faster than the theoretical ones, are probably caused by the azimuthal discrepancy (θ) between the incoming direction of tsunamis and the cable direction. When a plane wave with a propagation velocity obliquely impinges to the cable, the apparent velocity exceeds the propagation velocity ($c_a = c_p / \cos\theta$, where c_a and c_p is the apparent and phase velocities, respectively (Lior et al., 2021)). Using the phase velocity difference at each frequency, we calculated the azimuthal difference between the cable and the incoming direction, and obtained azimuthal differences of 10° – 30° (Figure 3b). Indeed, azimuthal differences between the cable directions and theoretically calculated ray paths for 10 mHz result in 0° – 40° at cable distances 0–50 km (Figure S1 in Supporting Information S1). The fact that the tsunami-related signals were observed at cable distances 0–65 km may be related to the azimuthal difference (θ) between the cable direction and incident azimuth of the tsunamis, because the DAS observation has an amplitude sensitivity of $\cos^2\theta$ (Kuvshinov, 2016; Mateeva et al., 2014). When tsunamis approach to shallow water depths, their propagation speeds are decelerated and the wavefront tends to be normal to coastlines. This indicates that tsunamis are possibly captured by DAS when submarine cables are installed perpendicular to the dipping direction of the seafloor topography.

3.2. Energy-Time Function

Figures 4 and S4 in Supporting Information S1 depict the estimated energy-time functions from the DAS and APG records. The amplitudes of each trace are normalized by their own RMS amplitudes. The highest peaks emerge between 21:00 and 21:30 at frequencies lower than 8 mHz, except for 6 mHz, while the largest peaks are identified at approximately 21:00 at frequencies higher than 14 mHz. In addition to those, distinct peaks appear at approximately 20:00 at frequencies higher than 14 mHz. This indicates that the energy of the excited tsunamis is shifted from high to low frequencies with time (Figures 4a and 4b). These features can be clearly recognized in both the APG and DAS records.

To interpret the obtained energy-time function for the tsunamis, we also construct similar energy-time functions of the repetitive T phases using high-frequency components of the OBSs. Figure 4c shows the normalized amplitudes of the envelope waveforms for the vertical component of the OBS with a bandpass filter of 30–40 Hz at MRA01 (Figure 4c). The distinct peaks correspond to the individual T phase events, and the waveform is time-shifted to the origin time using a propagation velocity of 1.47 km/s. Because the dominant frequency of T phases from earthquakes is typically 4–15 Hz, T phases with frequencies higher than 20 Hz and an impulsive peak are possibly associated with explosive eruption of submarine volcanic activities (Hammond & Walker, 1991). Sufficient high frequency components of the T phases as well as their sharp onsets detected in these events (right panel of Figure 4c) suggest that the T phases are triggered by submarine volcanic activities. A relatively large peak is excited at 20:00, then subsequent peak amplitudes tend to decrease until 21:00, while large peaks are again recorded at 21:00–21:30. The temporal variations in these peak amplitudes indicate that the submarine volcanic events started with small-sized eruptions and progressed to large-sized eruptions (Sandarbata et al., 2023).

The three peaks in the energy-time functions for the tsunamis are considered to be generated by either a single or multiple events that are identified by T phase peaks. Although it is unclear whether volcanic explosions are directly related to the tsunami generations, it is possible that smaller-sized volcanic activities generate a high-frequency tsunami peak at an earlier stage (20:00), and middle-frequency and low-frequency tsunami peaks are generated with increasing the volcanic-activity sizes at later stages (21:00–21:30). The earlier stage around 20:00 is consistent with the origin time estimated by fitting the frequency-dependent propagation time curve with dispersive signals (Figure 2a).

We obtained the resembling characteristics of the large tsunami peaks in the frequency-dependent energy-time functions between DAS and APG records, which suggests that DAS experiments alone can be used for not only tsunami detection but also elucidating the tsunami generation at the source location. Our study indicates that DAS records may be useful for complementing offshore tsunami information, particularly in the regions where other geophysical instruments are not available.

3.3. Strain Estimation

To estimate sea level changes using DAS records, it is necessary to understand what factors affect the DAS strain measurement. DAS potentially measures the strain originated from (I) the pressure variation of high-frequency

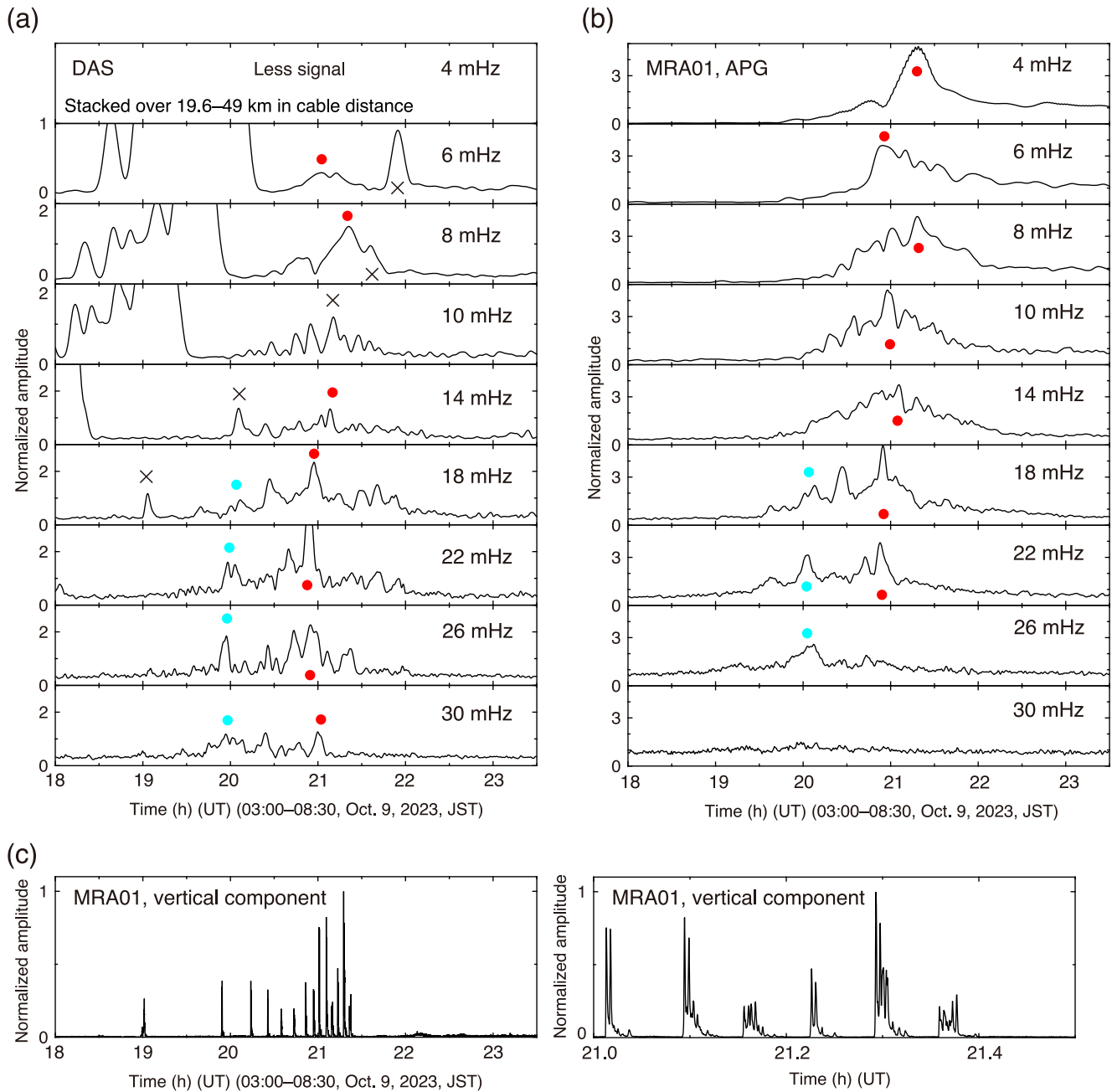


Figure 4. Energy-time functions estimated using DAS and APG records. (a) Stacked energy-time functions at each center frequency. The amplitudes of each trace are normalized by its RMS amplitude. Crosses indicate peaks that are produced by T-phase-generated site phenomena. Red and pale blue circles show possible peaks for later and earlier stages, respectively. (b) Same as panel (a), but for APG records observed at DONET. (c) The left panel shows the envelope waveform in the vertical component with a bandpass filter of 30–40 Hz at MRA01. Peaks correspond to repetitive T phases. The right panel shows the zoomed-up envelope waveform of the left panel.

tsunamis applied to the cable (pressure-induced length change of the fiber) (II) the seafloor deformation due to the tsunami pressure variation (deformation-induced strain), and (III) the temperature variation along cables (Figure S5 in Supporting Information S1). Although long-period components in the horizontal component of OBS typically incorporate not only the displacement but also tilt at the seafloor (Araki et al., 2004; Bell et al., 2015), DAS does not measure tilt. Here, long period components of DAS records, particularly tidal frequencies, are sensitive to temperature fluctuations along cables (Ide et al., 2021; Williams et al., 2022, 2023), and we do not

consider such effects in the frequency range of high-frequency tsunamis. It may be necessary to investigate the frequency dependence of the temperature effects to the strain of DAS measurements in future studies.

We roughly estimated the degrees of both (I) the pressure-induced length change and (II) the deformation-induced strain at a period range of 50–200 s, and compare the two components to the strain observed by DAS (Figure 3c). We refer to the approach of Kuvshinov (2016) for (I), and the idea of the horizontal compliance of Crawford (2004) for (II) (see details in Text S2 in Supporting Information S1). The obtained pressure-induced length changes are ranged between $4.17e-9$ and $2.25e-8$, and the obtained deformation-induced strains are between $6.79e-9$ and $2.04e-8$. Moreover, from the DAS records with the slant stacking technique, we obtained a strain due to the tsunamis of $1.11e-8 \pm 8.34e-9$. This value is comparable to both the pressure-induced length changes and the deformation-induced strains (Figure 3c), and the summation of the two types of the changes is comparable to or possibly exceeds the observed strain. This is probably caused by the ambiguities of the two estimated changes. Our results suggest that the two types of the changes may be incorporated comparably when submarine DAS experiments measure tsunami propagations, and that, if accurate information on cables and seafloor structures are obtained, sea level heights of high-frequency tsunamis can be obtained from DAS records. Here, the above estimations are based on the first order assumption, because seafloor cables may have complicated internal structures. In such cases, more cable-specific treatments may be useful.

4. Conclusions

We recorded high-frequency tsunamis (0.006–0.03 Hz) using DAS off the Cape Muroto, Japan. The dispersion feature of the tsunamis is consistent with that of IGWs, indicating that the observed signal corresponds to high-frequency tsunamis. As an application of the DAS measurement, we constructed the energy-time function of the tsunamis at the source location, which yielded waveforms comparable to those using APG records.

Future studies focus on (a) DAS observations of large tsunamis with low frequency components excited by earthquakes, (b) deployments of other geophysical instruments along the cable for low-frequency tsunami observations, and (c) their comparisons in terms of the amplitude difference and phase delay. Addressing such issues contribute to conducting DAS experiments for tsunami observations in regions with less other geophysical instrumentation.

Conflict of Interest

The authors declare no conflicts of interest relevant to this study.

Data Availability Statement

The DAS data that are used for reproducing the figures and that underlie the conclusion are available at Tonegawa (2023). APG and OBS data of DONET can be downloaded from NIED (<https://www.mowlas.bosai.go.jp/?LANG=en>). PDE catalog from USGS can be downloaded from the website (<https://earthquake.usgs.gov/earthquakes/search/>).

References

- Aoi, S., Asano, Y., Kunugi, T., Kimura, T., Uehira, K., Takahashi, N., et al. (2020). MOWLAS: NIED observation network for earthquake, tsunami and volcano. *Earth Planets and Space*, *72*(1), 126. <https://doi.org/10.1186/s40623-020-01250-x>
- Apel, J. R. (1987). *Principles of ocean physics*. Academic.
- Araki, E., Shinohara, M., Sacks, S., Linde, A., Kanazawa, T., Shiobara, H., et al. (2004). Improvement of seismic observation in the ocean by use of seafloor boreholes. *Bulletin of the Seismological Society of America*, *94*(2), 678–690. <https://doi.org/10.1785/0120020088>
- Baba, S., Araki, E., Yamamoto, Y., Hori, T., Fujie, G., Nakamura, Y., et al. (2023). Observation of shallow slow earthquakes by distributed acoustic sensing using offshore fiber-optic cable in the Nankai trough, southwest Japan. *Geophysical Research Letters*, *50*(12), e2022GL102678. <https://doi.org/10.1029/2022GL102678>
- Bell, S. W., Forsyth, D. W., & Ruan, Y. (2015). Removing noise from the vertical component records of ocean-bottom seismometers: Results from year one of the Cascadia initiative. *Bulletin of the Seismological Society of America*, *105*(1), 300–313. <https://doi.org/10.1785/0120140054>
- Cheng, F., Chi, B., Lindsey, N. J., Dawe, T. C., & Ajo-Franklin, J. B. (2021). Utilizing distributed acoustic sensing and ocean bottom fiber optic cables for submarine structural characterization. *Scientific Reports*, *11*(1), 5613. <https://doi.org/10.1038/s41598-021-84845-y>
- Crawford, W. C. (2004). The sensitivity of seafloor compliance measurements to sub-basalt sediments. *Geophysical Journal International*, *157*(3), 1130–1145. <https://doi.org/10.1111/j.1365-246X.2004.02264.x>
- Dziewonski, A., Bloch, S., & Landisman, M. (1969). A technique for the analysis of transient seismic signals. *Bulletin of the Seismological Society of America*, *59*(1), 427–444. <https://doi.org/10.1785/bssa0590010427>

Acknowledgments

We used OBS and APG data of DONET (doi:10.17598/nied.0008) operated by National Research Institute for Earth Science and Disaster Resilience (NIED). This work was partly supported by JSPS KAKENHI Grant JP21H05202, JP21H05204 in Scientific Research on Transformative Research Areas “Science of Slow-to-Fast earthquakes”.

- Ewing, W. M., & Worzel, J. L. (1948). Long-range sound transmission, Propagation of sound in the ocean. *Geological Society of America Memoir*, 27, 1–35.
- Fukushima, S., Shinohara, M., Nishida, K., Takeo, A., Yamada, T., & Yomogida, K. (2022). Detailed S-wave velocity structure of sediment and crust off Sanriku, Japan by a new analysis method for distributed acoustic sensing data using a seafloor cable and seismic interferometry. *Earth Planets and Space*, 74(1), 92. <https://doi.org/10.1186/s40623-022-01652-z>
- Hammond, S. R., & Walker, D. A. (1991). Ridge event detection: T-phase signals from the Juan de Fuca spreading center. *Marine Geophysical Researches*, 13(4), 331–348. <https://doi.org/10.1007/BF00366282>
- Ide, S., Araki, E., & Matsumoto, H. (2021). Very broadband strain-rate measurements along a submarine fiber-optic cable off Cape Muroto, Nankai subduction zone, Japan. *Earth Planets and Space*, 73(1), 63. <https://doi.org/10.1186/s40623-021-01385-5>
- Kaneda, Y., Kawaguchi, K., Araki, E., Matsumoto, H., Nakamura, T., Kamiya, S., et al. (2015). Development and application of an advanced ocean floor network system for megathrust earthquakes and tsunamis. In P. Favali, L. Beranzoli, & A. De Santis (Eds.), *SEAFLOOR OBSERVATORIES (vols. 1–Chapter 25)* (pp. 643–662). Springer Berlin Heidelberg. https://doi.org/10.1007/978-3-642-11374-1_25
- Kawaguchi, K., Kaneko, S., Nishida, T., & Komine, T. (2015). Construction of the DONET real-time seafloor observatory for earthquakes and tsunami monitoring. In P. Favali, L. Beranzoli, & A. De Santis (Eds.), *SEAFLOOR OBSERVATORIES (vols. 1–Chapter 10)* (pp. 211–228). Springer Berlin Heidelberg. https://doi.org/10.1007/978-3-642-11374-1_10
- Kuvshinov, B. N. (2016). Interaction of helically wound fibre-optic cables with plane seismic waves. *Geophysical Prospecting*, 64(3), 671–688. <https://doi.org/10.1111/1365-2478.12303>
- Lindsey, N. J., Dawe, T. C., & Ajo-Franklin, J. B. (2019). Illuminating seafloor faults and ocean dynamics with dark fiber distributed acoustic sensing. *Science*, 366(6469), 1103–1107. <https://doi.org/10.1126/science.aay5881>
- Lindsey, N. J., Rademacher, H., & Ajo-Franklin, J. B. (2020). On the broadband instrument response of fiber-optic DAS arrays. *Journal of Geophysical Research: Solid Earth*, 125(2), e2019JB018145. <https://doi.org/10.1029/2019JB018145>
- Lior, I., Mercerat, E. D., Rivet, D., Sladen, A., & Ampuero, J.-P. (2022). Imaging an underwater basin and its resonance modes using optical fiber distributed acoustic sensing. *Seismological Research Letters*, 93(3), 1573–1584. <https://doi.org/10.1785/0220210349>
- Lior, I., Sladen, A., Rivet, D., Ampuero, J., Hello, Y., Becerril, C., et al. (2021). On the detection capabilities of underwater distributed acoustic sensing. *Journal of Geophysical Research: Solid Earth*, 126(3), e2020JB020925. <https://doi.org/10.1029/2020JB020925>
- Mateeva, A., Lopez, J., Potters, H., Mestayer, J., Cox, B., Kiyashchenko, D., et al. (2014). Distributed acoustic sensing for reservoir monitoring with vertical seismic profiling. *Geophysical Prospecting*, 62(4), 679–692. <https://doi.org/10.1111/1365-2478.12116>
- Matsumoto, H., Araki, E., Kimura, T., Fujie, G., Shiraishi, K., Tonegawa, T., et al. (2021). Detection of hydroacoustic signals on a fiber-optic submarine cable. *Scientific Reports*, 11(1), 2797. <https://doi.org/10.1038/s41598-021-82093-8>
- Mizutani, A., & Melgar, D. (2023). Potential volcanic origin of the 2023 short-period tsunami in the Izu islands, Japan. *Seismica*, 2(2). <https://doi.org/10.26443/seismica.v2i2.1160>
- Nakano, M., Nakamura, T., Kamiya, S., Ohori, M., & Kaneda, Y. (2013). Intensive seismic activity around the Nankai trough revealed by DONET ocean-floor seismic observations. *Earth Planets and Space*, 65(1), 5–15. <https://doi.org/10.5047/eps.2012.05.013>
- NIED. (2019). *NIED DONET*. National Research Institute for Earth Science and Disaster Resilience. <https://doi.org/10.17598/nied.0008>
- NIED. (2023). Ocean bottom pressure data recorded by NIED DONET around Oct. 9, 2023 [Dataset]. *National Research Institute for Earth Science and Disaster Resilience*. <https://doi.org/10.17598/nied.0008-2023-001>
- Rawlinson, N., & Sambridge, M. (2004). Wave front evolution in strongly heterogeneous layered media using the fast marching method. *Geophysical Journal International*, 156(3), 631–647. <https://doi.org/10.1111/j.1365-246X.2004.02153.x>
- Sandanbata, O., Satake, K., Takemura, S., Watada, S., Maeda, T., & Kubota, T. (2023). Enigmatic tsunami waves amplified by repetitive source events near Sofugan volcano, Japan. *Geophysical Research Letters*, 51(2), e2023GL106949. <https://doi.org/10.1029/2023GL106949>
- Sipkin, S. A., Persion, W. J., & Presgrave, B. W. (2000). Earthquake Bulletins and catalogs at the USGS national earthquake information center: IRIS newsletter, v. 2000(1), p. 2–4.
- Sladen, A., Rivet, D., Ampuero, J. P., De Barros, L., Hello, Y., Calbris, G., & Lamare, P. (2019). Distributed sensing of earthquakes and ocean-solid Earth interactions on seafloor telecom cables. *Nature Communications*, 10(1), 5777. <https://doi.org/10.1038/s41467-019-13793-z>
- Smith, W. H. F., & Sandwell, D. T. (1997). Global sea floor topography from satellite altimetry and ship depth soundings. *Science*, 277(5334), 1956–1962. <https://doi.org/10.1126/science.277.5334.1956>
- Spica, Z. J., Ajo-Franklin, J., Beroza, G. C., Biondi, B., Cheng, F., Gaité, B., et al. (2023). PubDAS: A PUBLIC distributed acoustic sensing datasets repository for. *Geosciences*, 94(2), 983–998. <https://doi.org/10.1785/0220220279>
- Spica, Z. J., Castellanos, J. C., Viens, L., Nishida, K., Akuhara, T., Shinohara, M., & Yamada, T. (2022). Subsurface imaging with ocean-bottom distributed acoustic sensing and water phases reverberations. *Geophysical Research Letters*, 49(2), e2021GL095287. <https://doi.org/10.1029/2021GL095287>
- Spica, Z. J., Nishida, K., Akuhara, T., Pétréris, F., Shinohara, M., & Yamada, T. (2020). Marine sediment characterized by ocean-bottom fiber-optic seismology. *Geophysical Research Letters*, 47(16), e2020GL088360. <https://doi.org/10.1029/2020GL088360>
- Stern, R. J., Fouch, M. J., & Klemperer, S. L. (2003). An overview of the Izu-Bonin-Mariana subduction factory, inside the Subduction Factory. *Geophysical Monograph*, 138, 175–222. Copyright 2003 by the American Geophysical Union. <https://doi.org/10.1029/138GM10>
- 1992). Ocean Drilling Program, In B. Taylor, & K. Fujioka (Eds.) *Proceedings of the ocean drilling program, 126 scientific results* (Vol. 126). <https://doi.org/10.2973/odp.proc.sr.126.1992>
- Tonegawa, T. (2023). Data for spectrogram and waveforms [Dataset]. *Zenodo*. <https://doi.org/10.5281/zenodo.10434179>
- Tonegawa, T., Araki, E., Matsumoto, H., Kimura, T., Obana, K., Fujie, G., et al. (2022). Extraction of P Wave from ambient seafloor noise observed by distributed acoustic sensing. *Geophysical Research Letters*, 49(4), e2022GL098162. <https://doi.org/10.1029/2022GL098162>
- Tonegawa, T., Fukao, Y., Shiobara, H., Sugioka, H., Ito, A., & Yamashita, M. (2018). Excitation location and seasonal variation of transoceanic infragravity waves observed at an absolute pressure gauge array. *Journal of Geophysical Research: Oceans*, 123(1), 40–52. <https://doi.org/10.1002/2017JC013488>
- Viens, L., Bomilla, L. F., Spica, Z. J., Nishida, K., Yamada, T., & Shinohara, M. (2022). Nonlinear earthquake response of marine sediments with distributed acoustic sensing. *Geophysical Research Letters*, 49(21), e2022GL100122. <https://doi.org/10.1029/2022GL100122>
- Viens, L., Perton, M., Spica, Z. J., Nishida, K., Yamada, T., & Shinohara, M. (2023). Understanding surface wave modal content for high-resolution imaging of submarine sediments with distributed acoustic sensing. *Geophysical Journal International*, 232(3), 1668–1683. <https://doi.org/10.1093/gji/ggac420>
- Williams, C. M., Stephen, R. A., & Smith, D. K. (2006). Hydroacoustic events located at the intersection of the Atlantis (30°N) and Kane (23° 40'N) transform faults with the Mid-Atlantic ridge. *Geochemistry, Geophysics, Geosystems*, 7(6), Q06015. <https://doi.org/10.1029/2005GC001127>

- Williams, E. F., Fernández-Ruiz, M. R., Magalhaes, R., Vanthillo, R., Zhan, Z., González-Herráez, M., & Martins, H. F. (2019). Distributed sensing of microseisms and teleseisms with submarine dark fibers. *Nature Communications*, *10*(1), 5778. <https://doi.org/10.1038/s41467-019-13262-7>
- Williams, E. F., Ugalde, A., Martins, H. F., Becerril, C. E., Callies, J., Claret, M., et al. (2023). Fiber-optic observations of internal waves and tides. *Journal of Geophysical Research: Oceans*, *128*(9), e2023JC019980. <https://doi.org/10.1029/2023JC019980>
- Williams, E. F., Zhan, Z., Martins, H. F., Fernández-Ruiz, M. R., Martín-López, S., González-Herráez, M., & Callies, J. (2022). Surface gravity wave interferometry and ocean current monitoring with ocean-bottom DAS. *Journal of Geophysical Research: Oceans*, *127*(5), e2021JC018375. <https://doi.org/10.1029/2021JC018375>
- Wuestefeld, A., Spica, Z. J., Aderhold, K., Huang, H.-H., Ma, K.-F., Lai, V. H., et al. (2023). The global DAS month of february 2023. *Seismological Research Letters*, *95*(3), 1569–1577. <https://doi.org/10.1785/0220230180>
- Wuestefeld, A., & Wilks, M. (2019). How to twist and turn a fiber: Performance modeling for optimal DAS acquisitions. *The Leading Edge*, *38*(3), 226–231. <https://doi.org/10.1190/le38030226.1>
- Xiao, H., Spica, Z. J., Li, J., & Zhan, Z. (2024). Detection of earthquake infragravity and tsunami waves with underwater distributed acoustic sensing. *Geophysical Research Letters*, *51*(2), e2023GL106767. <https://doi.org/10.1029/2023GL106767>

References From the Supporting Information

- Brocher, T. M. (2005). Empirical relations between Elastic Wavespeeds and density in the Earth's crust. *Bulletin of the Seismological Society of America*, *95*(6), 2081–2092. <https://doi.org/10.1785/0120050077>
- Crawford, W. C., Webb, S. C., & Hildebrand, J. A. (1991). Seafloor compliance observed by long-period pressure and displacement measurements. *Journal of Geophysical Research*, *96*(B10), 16151–16160. <https://doi.org/10.1029/91JB01577>
- Daley, T. M., Miller, D. E., Dodds, K., Cook, P., & Freifeld, B. M. (2016). Field testing of modular borehole monitoring with simultaneous distributed acoustic sensing and geophone vertical seismic profiles at Citronelle, Alabama. *Geophysical Prospecting*, *64*(5), 1318–1334. <https://doi.org/10.1111/1365-2478.12324>
- Doran, A. K., & Laske, G. (2016). Infragravity waves and horizontal seafloor compliance. *Journal of Geophysical Research: Solid Earth*, *121*(1), 260–278. <https://doi.org/10.1002/2015JB012511>
- Takahashi, N., Kodaira, S., Nakanishi, A., Park, J.-O., Miura, S., Tsuru, T., et al. (2002). Seismic structure of western end of the Nankai trough seismogenic zone. *Journal of Geophysical Research*, *107*(B10), 1–2. <https://doi.org/10.1029/2000JB000121>
- Wang, H. F., Zeng, X., Miller, D. E., Fratta, D., Feigl, K. L., Thurber, C. H., & Mellors, R. J. (2018). Ground motion response to an ML 4.3 earthquake using co-located distributed acoustic sensing and seismometer arrays. *Geophysical Journal International*, *213*(3), 2020–2036. <https://doi.org/10.1093/gji/ggy102>